# In Search of The Optimal Atmospheric River Index for US Precipitation: A Multifactorial Analysis

**Chen Zhang**[1]**, Wen-wen Tung**[1]*****, William S. Cleveland**[2,3]

[1]Department of Earth, Atmospheric, and Planetary Sciences, Purdue University, West Lafayette, IN, USA

[2]Department of Statistics, Purdue University, West Lafayette, IN, USA

[3]Department of Computer Science, Purdue University, West Lafayette, IN, USA

**Key Points:**

- We searched for an optimal AR index based on the precipitation effects depending on regional physical mechanisms, seasons, and AR duration.
- *IWV* with 75th percentile climate threshold can capture the broad presence and accumulation of precipitation in both regions studied.
- Changing climatological threshold for detecting Midwest ARs results in a seasonal shift of maximum event-accumulated precipitation.

*****Department of Earth, Atmospheric, and Planetary Sciences, Purdue University, 550 Stadium Mall Drive, West Lafayette, IN 47907, USA

Corresponding author: Wen-wen Tung, `wwtung@purdue.edu`

**Abstract**

Atmospheric rivers (ARs) affect surface hydrometeorology in the US West Coast and Midwest. We systematically sought optimal AR indices for expressing surface precipitation impacts within the Atmospheric River Tracking Method Intercomparison Project (ARTMIP) framework. We adopted a multifactorial approach. Four factors—moisture fields, climatological thresholds, shape criteria, and temporal thresholds—collectively generated 81 West Coast AR indices and 81 Midwest indices from January 1980 to June 2017. Two moisture fields were extracted from the MERRA-2 data for ARTMIP: integrated water vapor transport ($IVT$) and integrated water vapor ($IWV$). Metrics for precipitation effects included two-way summary statistics relating the concurrence of AR and that of precipitation, per-event averaged precipitation rate, and per-event precipitation accumulation. We found that an optimal AR index for precipitation depends on the types of impact to be addressed, associated physical mechanisms in the affected regions, timing, and duration. In West Coast and Midwest, $IWV$-based AR indices identified the most abundant AR event time steps, most accurately associated AR to days with precipitation, and represented the presence of precipitation the best. With a lower climatological threshold, they detected the most accumulated precipitation with the longest event duration. Longer duration thresholds also led to higher accumulated precipitation, holding other factors constant. $IWV$-based indices are the overall choice for Midwest ARs under varying seasonal precipitation drivers. $IVT$-based indices suitably capture the accumulation of intense orographic precipitation on the West Coast. Indices combining $IVT$ and $IWV$ identify the fewest, shortest, but most intense AR precipitation episodes.

**Plain Language Summary**

[Atmospheric rivers (AR), the long narrow filaments of enhanced water vapor transport in the lower troposphere, are known to accompany extreme rain and winds. They are important weather systems for US water resources on the West Coast and in the Midwest. In our study, we asked which impacts, in which region, and in what time scale and period were of concern. We then used an approach combining climate significant- or extreme-event criteria, image processing, and statistical analysis to create 81 West Coast AR indices and 81 Midwest indices from January 1980 to June 2017 for answering the questions with detailed visualization. We found that an optimal AR index for precipitation

depends on the defined precipitation impacts, regional physical mechanisms of precipitation, season, and duration. Integrated water vapor ($IWV$) can represent the broadstroke presence and accumulation of precipitation in regions studied. Longer duration thresholds also led to higher accumulated precipitation. Combined moisture with wind fields using integrated water vapor transport ($IVT$), is necessary to get extreme West Coast AR orographic precipitation. $IWV$ well represents moderate to extreme Midwest AR precipitation events for all seasons. Combination of $IVT$ and $IWV$ is useful to get snapshots of extreme precipitation events.]

## 1 Introduction

Atmospheric rivers (ARs) are long, narrow filaments of enhanced water vapor transport that is typically associated with a low-level jet and extratropical cyclone (Ralph et al., 2018). When these moisture-laden ARs make landfall or penetrate inland, water vapor condenses and can release enhanced precipitation (e.g., Guan et al., 2010, 2013; Luo & Tung, 2015). AR precipitation in many parts of the world is paramount for water resources (e.g., Guan et al., 2010; Dettinger et al., 2011; Rutz & Steenburgh, 2012; Dettinger, 2013; Lavers & Villarini, 2015; Eiras-Barca et al., 2016; Blamey et al., 2018; Little et al., 2019). However, heavy rainfall can lead to floods and ensuing socioeconomic damage. Studies have shown that in North America, ARs have significant surface hydrometeorological effects on the western North America (e.g., Ralph et al., 2006; Neiman et al., 2008; Leung & Qian, 2009; Ralph et al., 2011; Dettinger, 2011; Rutz et al., 2014; X. Chen et al., 2018) and the US Midwest (e.g., Lavers & Villarini, 2013; Nayak & Villarini, 2017).

The first and critical task to study ARs is to develop AR identification methods. There have been many AR detection and tracking methods for different purposes in the literature, as noted in the Atmospheric River Tracking Method Intercomparison Project (ARTMIP, Shields et al., 2018; Rutz et al., 2019; O'Brien et al., 2020). These different detection methods are primarily based on either one or both measurements of Integrated Water Vapor ($IWV$) and Integrated Water Vapor Transport ($IVT$).

Ralph et al. (2004, 2005, 2006) created an objective AR identification method using satellite-based $IWV$ for case studies in the North American West Coast. They defined ARs with $IWV$ content $> 20$ mm, length $> 2000$ km, and width $< 1000$ km. Sim-

77 ilar approaches have since been widely applied (e.g., Neiman et al., 2008; Wick et al.,

78 2013). Furthermore, $IVT$ derived from reanalysis or models incorporates the effects of

79 advection. Zhu and Newell (1998) first defined ARs through $IVT$. Lavers et al. (2012)

80 and Lavers and Villarini (2013), respectively, established percentile-based $IVT$ thresh-

81 olds to study ARs affecting Britain and Central US. Guan and Waliser (2015) applied

82 85th percentile seasonal climatological thresholds to $IVT$ for global AR detection. Mean-

83 while, Rutz et al. (2014) used absolute thresholds, preferring $IVT \geq 250$ kg m$^{-1}$ s$^{-1}$ to

84 $IWV \geq 20$ mm as a threshold to emphasize inland-penetrating ARs in the Western US.

85 $IVT$-based detection method is increasingly chosen over $IWV$-based ones in re-

86 search and operation as horizontal moisture transport is qualitatively related with oro-

87 graphic precipitation (e.g., Neiman et al., 2009; Rutz et al., 2014; Guan & Waliser, 2015).

88 The combination of $IVT$ and $IWV$ ($IVT+IWV$ thereafter) was recently adopted (e.g.,

89 Eiras-Barca et al., 2016; Gershunov et al., 2017). The $IVT + IWV$ method was pro-

90 posed to reduce erroneous detection of ARs from considering only one of the measure-

91 ments (Eiras-Barca et al., 2016). It requires both $IVT$ and $IWV$ values to meet their

92 corresponding thresholds simultaneously.

93 Furthermore, the duration of an AR is important for its hydrometeorological ef-

94 fects. Longer-lived ARs are more likely to bring higher rainfall (in total and on average)

95 and streamflow than shorter-duration ones (Ralph et al., 2013; Nayak & Villarini, 2018).

96 However, there has not been a consensus in duration criteria. Duration thresholds were

97 not used in some early case studies (e.g., Ralph et al., 2004). Subsequently, a minimum

98 of at least 8 (Ralph et al., 2013), 12 (Payne & Magnusdottir, 2016), 18 (Lavers et al.,

99 2012; Lavers & Villarini, 2013; Nayak & Villarini, 2017; Gershunov et al., 2017), or 24

100 consecutive hours (Sellars et al., 2015) were included as a part of detection algorithms.

101 Although systematic comparisons among different AR identification methods are

102 underway (Shields et al., 2018; Rutz et al., 2019; Ralph et al., 2019), the relationships

103 between the methods and associated AR precipitation remain to be quantified. Impor-

104 tant questions to ask include: between the two common detection measurements of $IVT$

105 and $IWV$, which one, or both, should be used when surface precipitation is concerned?

106 How do more restrictive duration criteria perform if long-lived ARs produce larger amounts

107 of precipitation than short-lived ones (Ralph et al., 2013)? In probing these questions,

108 we attempted to establish an optimal AR detection algorithm suited for expressing sur-

face precipitation impacts. We used a multi-factorial ensemble analysis, well suited for uncertainty quantification, focusing on the percentile-based approaches within the ART-MIP framework of prevailing detection methods and reanalysis data from January 1980 to June 2017. The paper is organized as follows: data and methods are in section 2. Surface precipitation effects associated with different AR detection indices are analyzed and discussed in section 3. Sections 4 and 5 provide discussions and conclusions, respectively.

## 2 Data and Methods

### 2.1 Data

#### 2.1.1 MERRA-2 data for ARTMIP

The two conventional moisture measurements for AR detection, $IVT$ and $IWV$, were extracted from the Modern-Era Retrospective analysis for Research and Applications, Version 2 (MERRA-2) source data for ARTMIP through Climate Data Gateway (NCAR CDG, 2019). This dataset was calculated by the Center for Western Weather and Water Extremes at the University of California, San Diego, according to the following formula (Shields et al., 2018):

$$IVT \;\; = \;\; -\frac{1}{g}\int_{1000}^{200} q(p)|\mathbf{V}_{\mathrm{h}}(p)| \; dp, \tag{1}$$

$$IWV \;\; = \;\; -\frac{1}{g}\int_{1000}^{200} q(p) \; dp \tag{2}$$

The three variables, horizontal wind ($\mathbf{V}_{\mathrm{h}} = (u, v)$ where $u$ is the zonal and $v$ the meridional winds in m s$^{-1}$), specific humidity ($q$ in kg kg$^{-1}$), and pressure ($p$ in hPa), used in the formula were from NASA MERRA-2 (Gelaro et al., 2017). The horizontal spatial resolution and temporal resolution of the vertically integrated fields are 0.5° longitude by 0.625° latitude and 3 hours. We used all of the MERRA-2 Tier 1 data available at the time of download, from January 1980 to June 2017, to create climatological thresholds. Then, we applied the AR detection algorithm to the dataset to generate AR indices.

### *2.1.2 CPC US Unified Precipitation Data*

The NOAA Climate Prediction Center (CPC) Unified Gauge-Based Analysis of Daily
Precipitation over the Contiguous United States (hereafter, CPC) provides daily precip-
itation on a fine-resolution (0.25° latitude by 0.25° longitude) from January 1948 to the
present (Higgins et al., 2000; Xie et al., 2007; M. Chen et al., 2008). Gibson et al. (2019)
evaluated this product and found overall good agreement with the in-situ Parameter-
Elevation Regressions on Independent Slopes Model (PRISM) dataset (Daly et al., 2008).
As described in the next subsection, these AR indices were defined by various AR de-
tection criteria applied to the ARTMIP MERRA-2 data. Their original spatial and tem-
poral resolutions are those of the MERRA-2. We spatially interpolated the coarser AR
index values (0 or 1) with bilinear interpolation to the CPC data's finer mesh, then rounded
off the results to integers. Each CPC daily precipitation measurement was divided evenly
over the twenty-four hours centered at 00 UTC, then aggregated into the AR indices'
3-hourly intervals.

### 2.2 AR Detection Algorithm

As shown in Figure 1, we used 4 factors—moisture fields, climatological thresholds,
shape criteria, and temporal thresholds—to generate an ensemble of 81 AR indices for
the US West Coast and 81 for the Midwest. First, we used $IVT$, $IWV$, or $IVT+IWV$
as the moisture field. Then, for each grid point, we selected moisture field values at 1200
UTC every day during neutral or weak El Niño–Southern Oscillation (ENSO) events from
January 1980 to June 2017. We called these test values. Here, we adopted the bi-monthly
NOAA Multivariate ENSO index (MEI.v2, e.g., Wolter & Timlin, 1993) and preserved
only test values in the months when the MEI.v2 index was within $\pm1$. Three monthly
climatological thresholds were calculated for each set of test values—$IVT$, $IWV$, or $IVT+$
$IWV$—at each grid point. In addition to the common 85th percentile (e.g., Lavers et
al., 2012; Lavers & Villarini, 2013; Guan & Waliser, 2015; Eiras-Barca et al., 2016), we
also used the 75th and the 95th percentiles as thresholds. Consequently, at any given
grid point and time, a moisture value equal to or exceeding a threshold suggests the po-
tential presence of AR.

Figure 2 plots these three levels of climatological thresholds of $IVT$ and $IWV$ fields
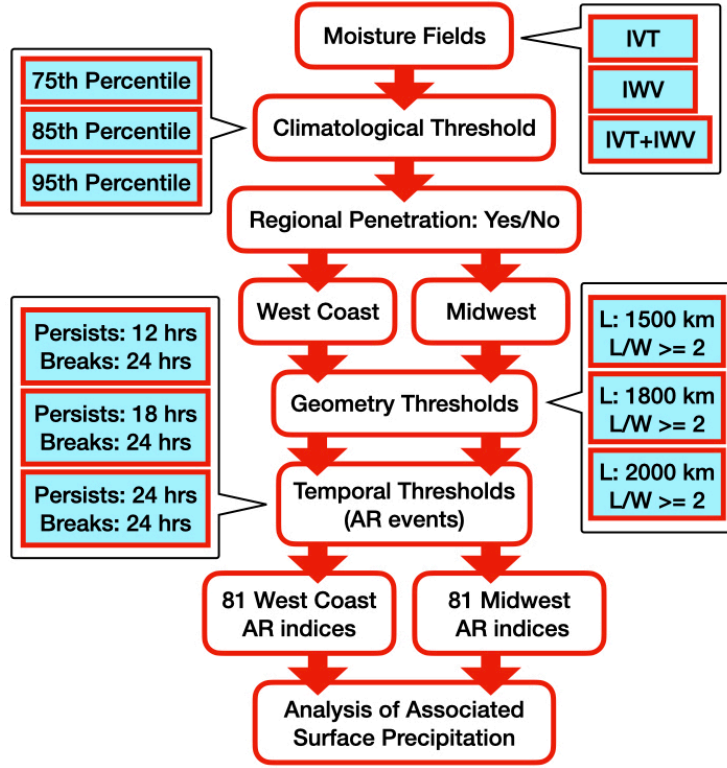over North America for January and August. The threshold at each grid point elevates

**Figure 1.** Schematic diagram illustrating the multifactorial AR detection algorithm.

successively, increasingly restricting AR detection, from 75th to 95th percentile. The $IVT$ maxima corresponded to extratropical storm tracks and ITCZ over the North Pacific and the North Atlantic. The $IWV$ maxima co-located with tropical and extratropical warm oceans as well as maritime tropical air mass. Consistent with Clausius–Clapeyron equation, $IVT$ and $IWV$ thresholds were generally higher in the summer (August) than in the winter (January). To relate identified ARs with surface precipitation effects, we defined the regions of West Coast and Midwest based on the boundaries of CPC precipitation data. The regions of the West Coast (situating between 33°–48.5° N and 124.375°– 114.375° W) and Midwest (between 37°–47° N and 94°–84° W) are outlined in red. This seasonal difference was more evident in the Midwest than the West Coast. Regardless, the $IVT$ maximum over the Northeast Pacific Ocean expanded towards the West Coast in January, then retreated in August.

Figure 2 also compares the monthly percentile thresholds in this study against the absolute thresholds used by Gershunov et al. (2017), defined as 250 kg m$^{-1}$s$^{-1}$ in $IVT$ and 15 kg m$^{-2}$ in $IWV$. The monthly percentile thresholds exhibit more spatial details
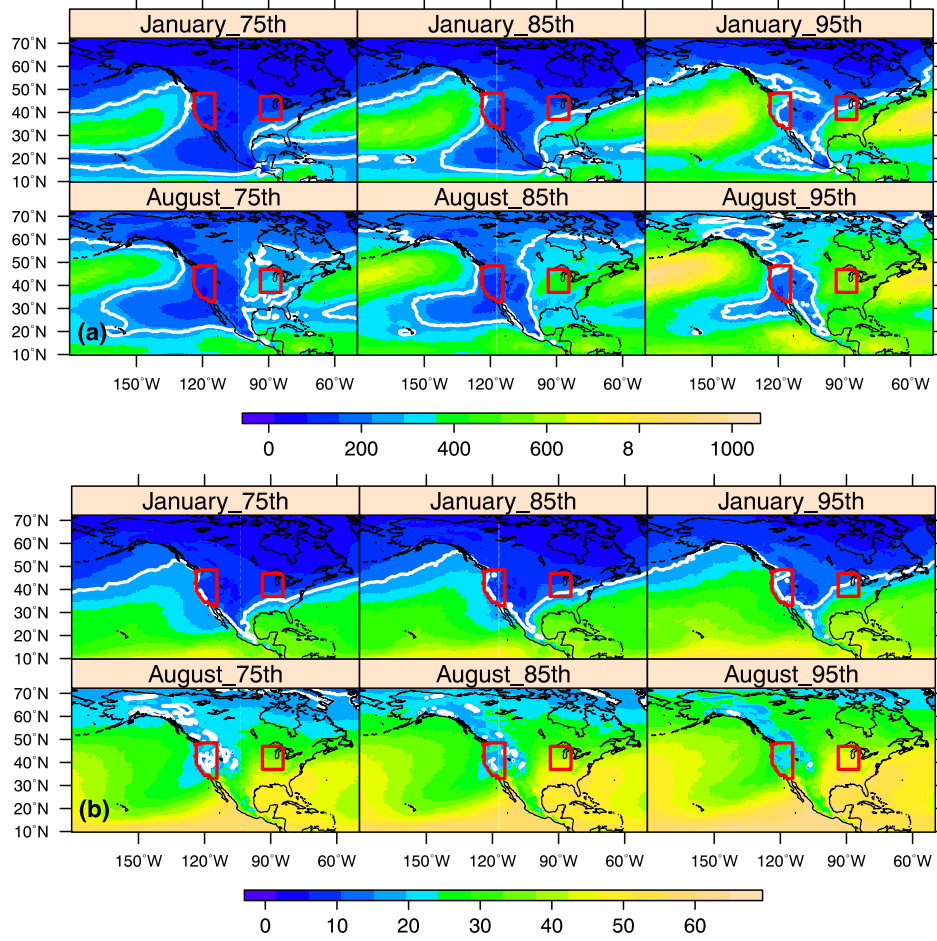
**Figure 2.** Three levels (75th, 85th, and 95th) of climatological thresholds of $IVT$ (a, kg m$^{-1}$s$^{-1}$) and $IWV$ (b, kg m$^{-2}$) over North America for January and August derived from neutral or weak ENSO events between January 1980–June 2017. The red boxes outline the West Coast and Midwest regions in this study. White lines (250 kg m$^{-1}$s$^{-1}$ in $IVT$ and 15 kg m$^{-2}$ in $IWV$) are the absolute thresholds in Gershunov et al. (2017).

as well as seasonal variability than the absolute ones. Through visual inspection, one can infer the different outcomes of AR detection if solely based on these thresholds. In January, absolute $IVT$ and $IWV$ thresholds resulted in fewer instances of landfalling ARs in both West Coast and Midwest compared with the respective 75th and 85th percentile thresholds. This is because the majority of the monthly percentile threshold values in these two regions are below the absolute thresholds. The absolute thresholds, however, permitted more frequent January AR detection along the West Coast and southern Midwest than the 95th percentile threshold values. These were also true for West-Coast AR detection using $IVT$ in August; however, in the Midwest, the absolute $IVT$ threshold was less restrictive to August AR detection than all $IVT$ monthly percentiles. The absolute $IWV$ threshold allowed overall more August AR detection than the monthly percentiles in the plotted domain.

The variability of AR detection across various thresholds above attests to the necessity of additional constraints. At each time step, we identified the grid points whose $IVT$ or $IWV$ values exceeded their corresponding climatological thresholds and kept only the data of those making landfall in the West Coast or penetrating into the Midwest. Then, we used the principal curves method (Hastie & Stuetzle, 1989) to determine the length of the curvy patterns formed by aggregating the maximum $IVT$ or $IWV$ values at each latitude and longitude. The width was calculated as the total Earth surface area of the identified grid points divided by the length. The geometry thresholds were further applied. A subset of potential AR data was extracted if a length was greater or equal to 1500, 1800, or 2000 km while the ratio of length to width was greater or equal to 2 (Figure 1). It is noted that, for the detection of West Coast land-falling ARs, this length was estimated using only the segment of data over the Pacific; for the ARs penetrating into the Midwest, it was estimated using the entire segment. The subsets of data were further filtered and aggregated into AR events that persisted for equal to or more than 12, 18, or 24 hours with breaks shorter than 24 hours within an event. The length of break criterion was based on Lavers and Villarini (2013).

At this point, 81 members of AR indices for each of the West Coast and Midwest regions from January 1980 to June 2017 were completed. Each index identifies the spatial and temporal information of AR events that satisfied one of the 81 combinations of the criteria form by the four factors. We proceeded with systematic analysis of the relationships between these ARs and surface precipitation in the West Coast and the Mid-
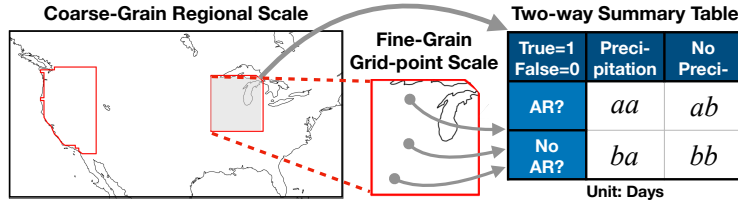
**Figure 3.** A two-way summary table with the terms for evaluating AR indices' relationships with surface precipitation on coarse- and fine-grain scales.

west. The AR detection and detailed analysis were executed via distributed-parallel computing on a high-performance computing cluster with Hadoop system in the backend and the R language-based DeltaRho software in the frontend (Cleveland & Hafen, 2014; Tung et al., 2018).

### 2.3 Coarse- to Fine-Grain Two-Way Summary Table

We built a two-way summary table (Figure 3) to explore the relationships between ARs identified by the indices and the surface precipitation in the West Coast and the Midwest. We took two spatial scales into account: regional coarse-grain scale and grid-point fine-grain scale. On the coarse-grain scale, we regarded either West Coast or Midwest as one entity. Within each entity, days centered at 00 UTC with at least one AR time step identified in a 3-hourly AR index were defined as AR days. Days without any AR time steps were considered as no AR days. Precipitation was based on the CPC US Unified Precipitation Data. The *aa* in the summary table was total AR days with precipitation; the *ab* was AR days without precipitation; the *ba* was days with no ARs but with precipitation; and the *bb* was days with no ARs and no precipitation.

From the summary table, four statistics were derived: *AR Related Precipitation*, *Precision*, *Accuracy*, and *F1 score*. The names loosely follow those in statistical classification (e.g., Hastie et al., 2001). However, the statistics here did not validate any predictive modeling of precipitation.They were used to compare the MERRA-2 AR indices' performance of relating to CPC surface precipitation effects. They may, however, provide empirical upper limits of a predictive model using only an AR index to predict precipitation within the data, spatial, and temporal domains in the study. *AR Related Pre-*

235    *cipitation* is defined as

$$\frac{aa}{aa+ba} = \frac{aa}{D_P},\tag{3}$$

237    with $D_P$ the total days with precipitation. It specifies how often surface precipitation,

238    if existed, was related to the ARs identified by an index. In predictive modeling, *AR Re-*

239    *lated Precipitation* is called *Sensitivity* in statistics or *Probability of Detection* in weather

240    forecast. *Precision* is defined as

$$\frac{aa}{aa+ab} = \frac{aa}{D_{AR}},\tag{4}$$

242    with $D_{AR}$ the total days with ARs according to an index. It describes how often the de-

243    tected ARs were actually related with precipitation. In weather forecast, *Precision* equals

244    to 1-*False Alarm Ratio*. *Accuracy* is defined as

$$\frac{aa+bb}{aa+ab+ba+bb} = \frac{aa+bb}{D},\tag{5}$$

246    with $D$ the total 13695 days in the data. For each AR index, it measures how often days

247    with/without ARs were correctly associated with precipitation/no precipitation. The $F1$

248    *score*,

$$\frac{2*AR\ Related\ Precipitation*Precision}{AR\ Related\ Precipitation + Precision},\tag{6}$$

250    is the harmonic mean of *AR Related Precipitation* and *Precision*. An AR index with a

251    low $F1$ *score* has both poor *AR Related Precipitation* and poor *Precision*, therefore an

252    overall poor AR-precipitation relation.

253        Each of these four statistics had one resultant value for each index on the coarse-

254    grain scale in either West Coast or Midwest. On the fine-grain scale, they were multi-

255    plied by the number of grid points inside a region: 2069 in the West Coast and 1508 in

256    the Midwest. The different sample sizes were taken into account in interpreting the re-

257    sults (section 3.2).

## 3 Analysis and Results

### 3.1 Identified AR occurrence summary statistics

260        Figures 4 and 5 visualize three summary statistics of AR occurrence obtained with

261    162 AR indices. These figures are Cleveland dotplots (Cleveland & McGill, 1984) cre-

262    ated in the Trellis display framework (Becker et al., 1996). The number of AR events

(Figure 4a), the accumulated time of these events measured in 3-hourly time steps (Figure 4b), and the average duration per event in days (Figure 5) are plotted on each panel, conditional on 18 combinations of regions (West Coast or Midwest), moisture fields ($IVT$, $IWV$, or $IVT+IWV$), and AR length criteria (1500, 1800, or 2000 km). The results are 18 packets, or subsets, of values. Each packet has 9 paired values of a summary statistic in the $y$-axis and one of the AR persistent duration thresholds (12, 18, or 24 hours along the $x$-axis), grouped with color by climatological thresholds (75th, 85th, or 95th percentiles).

Figure 4a shows that, from January 1980 to June 2017, each 75th and 85th percentile climatological threshold-based AR index captured $O(1000)$ events in either West Coast or Midwest regions, except for a few $IVT+IWV$-based ones with the most restrictive combinations of length and persistent duration criteria in the West Coast. In Figures 4b and 5, $IWV$-based indices identified the most AR time steps and longest average per-event duration; $IVT+IWV$-based indices identified the least and the shortest. Note that the per-event duration of each AR event was calculated as the summation of persistent AR time segments, excluding the break times. Increasing the restrictiveness of climatological threshold from 75th to 95th percentile while holding other factors constant, the number of identified AR time steps decreased dramatically, so did the average duration per event.

However, more restrictive climatological thresholds did not always yield fewer AR events (Figure 4a). Among $IVT$- and $IWV$-based Midwest AR indices, the 85th percentiles permitted more AR events but fewer time steps than the 75th percentiles, owing to the latter's tendency to yield longer per-event durations (Figure 5). Furthermore, the identified Midwest ARs had overall more total time steps than that of West-Coast ARs (Figure 4b). Midwest ARs had longer average per-event durations than those in the West Coast; the differences were the largest at the 75th percentiles and the least at the 95th percentiles (Figure 5).

In Figures 4 and 5, the effects of length criteria were only secondary to climatological thresholds. However, increasing the thresholds of AR persistent duration from 12 to 24 hours resulted in shorter accumulated time steps (Figure 4b) and, in most cases, longer average per-event duration (Figure 5) of the identified ARs. It also led to decreasing AR event counts (Figure 4a).
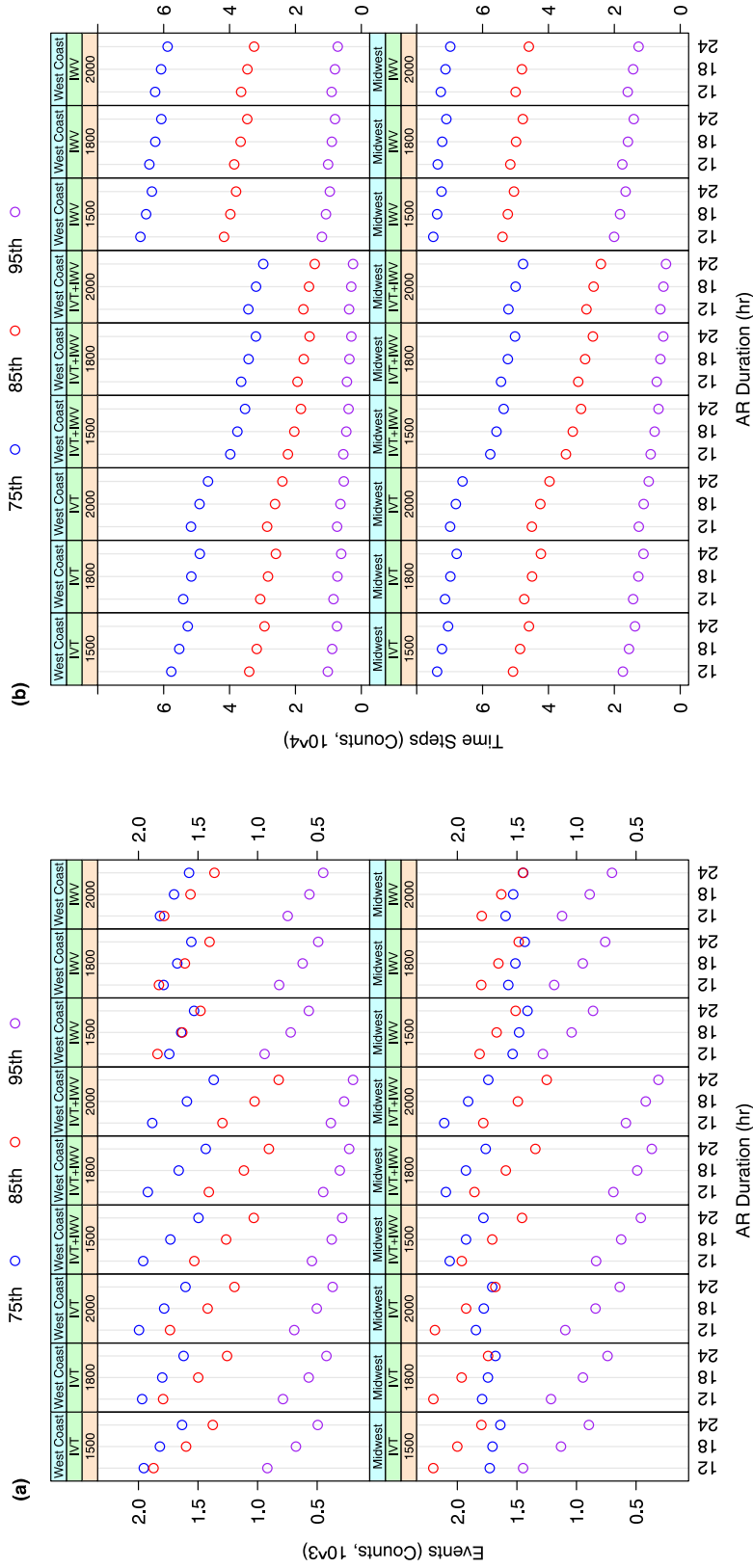
**Figure 4.** Numbers of (a) AR events (counts) and (b) accumulated AR time steps (counts) identified by 81 West-Coast (top row) and 81 Midwest (bottom row) AR indices. Each figure has 18 packets, or subsets of values conditional on 18 combinations of regions (West Coast or Midwest in blue boxes), moisture fields (*IVT*, *IWV*, or *IVT* + *IWV* in green boxes), and AR length criteria (1500, 1800, or 2000 km shown in yellow boxes). Each packet has 9 paired values of a summary statistic in the *y*-axis and one of the AR persistent duration criteria (12, 18 and 24 hours along the *x*-axis), grouped by color into three levels of climatological thresholds (75th, 85th, and 95th percentiles shown respectively in blue, red, and purple).
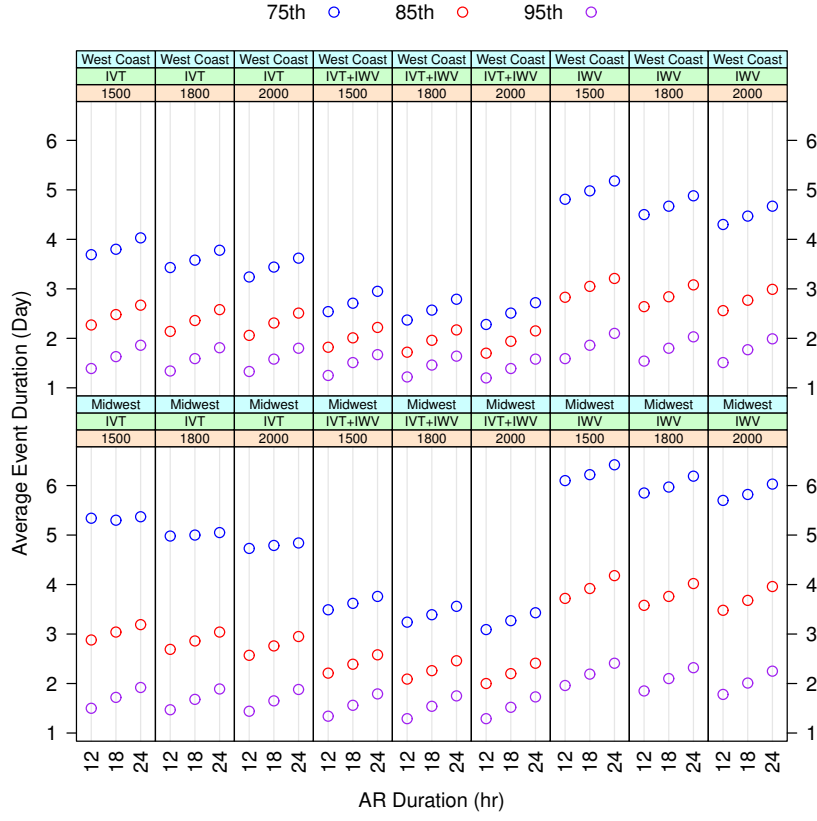
**Figure 5.** Similar to Figure 4, but for average per-event duration (unit: Day) identified by 81 West-Coast (top row) and 81 Midwest (bottom row) AR indices.

295   **3.2   Coarse- to fine-grain daily AR-precipitation occurrence relation anal-**

296       **ysis**

297   *3.2.1   Coarse-grain analysis*

298       At the outset, we aimed to identify the AR indices that represent the precipitation

299   occurrence as complete and correct as possible. Figure 6a shows the coarse-grain *Accu-*

300   *racy* in dotplots. An *Accuracy* of 1 means there was precipitation if and only if ARs were

301   detected by an index. In general, indices associated with more AR time steps (Figure 4b)

302   also exhibited higher *Accuracy* at the coarse-grain scale. Indeed, Midwest ARs bore higher

303   *Accuracy* than the West Coast ARs given otherwise the same factors. The *IWV*-based

304   AR indices yielded the highest *Accuracy* in both regions. Among them, indices using the

305   75th percentile climate threshold had *Accuracy* exceeding 0.64 in the West Coast and

306   0.74 in the Midwest. More restrictive climatological thresholds resulted in lower *Accu-*

307   *racy*. The lowest values were within the 95th-percentile-based *IVT* + *IWV* indices—

308   below 0.09 for the West Coast and 0.14 for the Midwest ARs. More restrictive length

309   and temporal criteria that detected fewer AR events or time steps also depressed *Accu-*

310   *racy* values, while the effect of length was minor in comparison to other factors.

311       Figure S1 shows the *AR Related Precipitation*, *i.e.,* the fraction of total days with

312   precipitation attributable to identified ARs. It has a very similar pattern to Figure 6a.

313   In particular, when 75th-percentile *IWV*-based indices were used, more than 64% and

314   74% of precipitation days occurred in the presence of ARs in the West Coast and Mid-

315   west, respectively. However, 95th-percentile *IVT+IWV*-based indices could only cap-

316   ture less than 9% and 14% of precipitation days in the respective regions. On the other

317   hand, *Precision* values in Figure S2 display a very different pattern from Figures 6a or

318   S1. For the West Coast landfalling ARs, 21 out of 81 indices had *Precision* equal to 1,

319   with the rest approximately 1. That means each index very precisely associated AR days

320   with precipitation. For ARs influencing the Midwest, the *Precision* values were slightly

321   smaller but still larger than 0.998.

322       The *F*1 *score*s in Figure 6b summarizes for each AR index the combined perfor-

323   mance of relating to the presence of precipitation (*Precision*) and explaining the occur-

324   rence of precipitation (*AR Related Precipitation*) at the coarse-grain scale. Unlike *Ac-*

325   *curacy*, *F*1 *score* does not consider days with no AR and no precipitation, expressed as

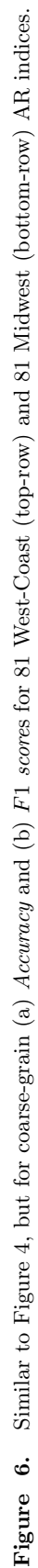326   the *bb* term in (5). In practice, we are more concerned about the relationship between

327  the presence of AR and that of precipitation than the absence of both. Therefore, $F1$

328  *score* is a more sensible measurement than *Accuracy*. Furthermore, the score could be

329  considered as adjusted *Precision*, with which indices gained high *Precision* via narrow-

330  ing to extreme samples are penalized. The adjustment differentiated the overall high *Pre-*

331  *cision* values (Figure S2) to the pattern of $F1$ *score*s (Figure 6b), which resembles Fig-

332  ures 6a and S1 but have larger magnitudes across the board.

### 3.2.2 Fine-grain analysis

334  We established for each index a two-way summary table for each individual grid

335  point in West Coast and Midwest for fine-grain analysis. The distributions of fine-grain

336  $F1$ *score*s are summarized using boxplots for the 81 West Coast AR indices, each with

337  2069 points (Figure 7a) and 81 Midwest indices with 1508 points (Figure 7b).

338  In Figure 7a, the interquartile ranges (IQR) of the 81 $F1$ distributions, as indicated

339  by the box lengths, vary from ∼0.017 to ∼0.089 for the West Coast AR indices. Spa-

340  tial inhomogeneity of precipitation captured by different indices contributed to this vari-

341  ation. Another important influencer was the different AR days, $D_{AR}$, as inferred by the

342  AR time steps (Figure 4b), resulted from different indices. Indeed, the smaller IQRs are

343  seen among the most restrictive indices with the fewest AR time steps, such as the 95th-

344  percentile $IVT + IWV$-based ones. Moreover, the minimum, first quartile (Q1), sec-

345  ond quartile/median (Q2), third quartile (Q3), and maximum of each subset of $F1$ *score*s

346  decrease with more restrictive criteria. This is consistent with the coarse-grain analy-

347  sis (Figure 6b). When the climate threshold, length, and time criteria were fixed, the $IWV$-

348  based indices slightly outperformed $IVT$-based ones and were significantly better than

349  $IVT + IWV$-based ones. The 75th-percentile $IWV$-based indices yielded the largest

350  median $F1$ *score*s, all exceeding 0.5.

351  The IQRs of fine-grain $F1$ *score* distributions for the 81 Midwest AR indices (Fig-

352  ure 7b) are smaller than those for West Coast AR indices (Figure 7a). This is most cer-

353  tainly due to the ∼30% smaller sample size in the Midwest than that of the West Coast.

354  The differences among the $F1$ *score* distributions in the Midwest are qualitatively sim-

355  ilar to those in the West Coast. Nevertheless, the $F1$ *score*s in the Midwest are overall

356  higher. The 75th-percentile $IWV$-based indices struck the highest median $F1$ *score*s at

357  ∼0.65. These are consistent with the coarse-grain $F1$ analysis (Figure 6b).

**Figure 6.** Similar to Figure 4, but for coarse-grain (a) *Accuracy* and (b) *F1 scores* for 81 West-Coast (top-row) and 81 Midwest (bottom-row) AR indices.
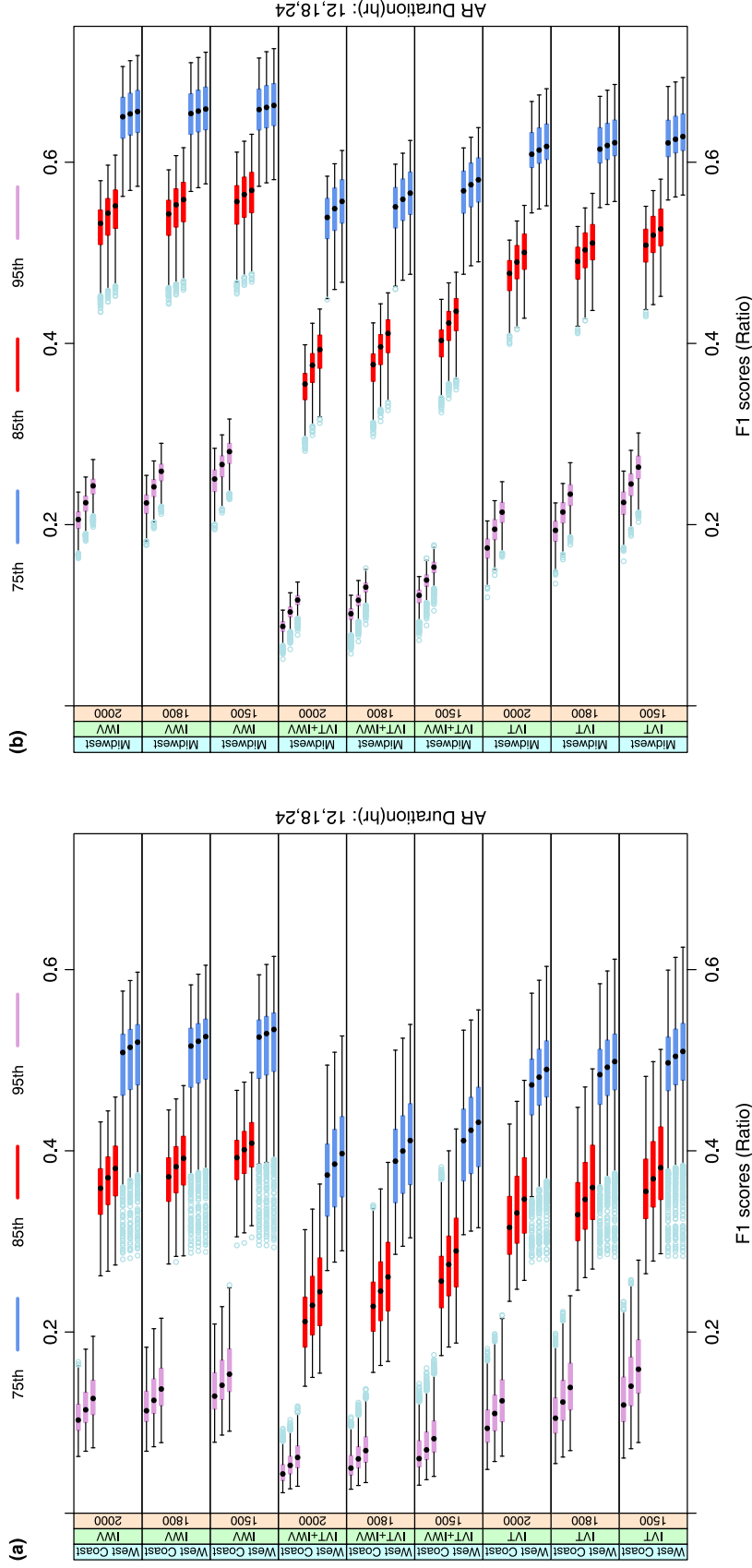
**Figure 7.** Boxplots of fine-grain *F1 scores* for the (a) West Coast and (b) Midwest AR indices. Each figure has nine packets from combinations of three moisture (*IVT*, *IWV*, or *IVT* + *IWV*) and three AR length criteria (1500, 1800, or 2000 km). Each packet has nine boxplots grouped by color into three levels of climatological thresholds (75th, 85th, or 95th percentile). Within each triplet, from bottom to top, the persistent duration thresholds increase from 12, 18, to 24 hours. Each boxplot includes the colored box spanning from Q1 to Q3 of the distribution, a black dot marking the median, and the whiskers. The whiskers extend to the most extreme data point that is no more than 1.5 times the length of the box (IQR) away from the box. Any data points outside the whiskers are marked as potential outliers in light blue.

### 3.3 Deep Analysis at the Finest Granularity

In section 3.2, we studied the presence or absence of ARs in relation to those of precipitation, as reflected by the ensembles of indices in the North American West Coast and the US Midwest. Past studies consistently showed that in general, ARs contributed to a fair amount of annual precipitation—up to 50% depending on the location—in the contiguous United States (Dettinger et al., 2011; Rutz & Steenburgh, 2012; Lavers & Villarini, 2015; Nayak & Villarini, 2017). Hence, in the next step, we analyzed the amount of AR-related precipitation associated with different indices. We quantified precipitation impacts with event-average rate (3.3.1) and event-accumulated precipitation (3.3.2 and 3.3.3) and compared them across the AR indices.

#### 3.3.1 Event-Average Surface Precipitation Effects

For each AR index, we tracked the surface area of an AR at each recorded time step. We then calculated the areal-averaged surface precipitation rate at each time step. The event-average surface precipitation rate was calculated as the event time-mean of areal averages. As an example, Figure 8 compares the event-average precipitation rate across a group of AR indices with the 1500-km length and 18-hr persistent duration criteria using boxplots, conditional on locations, climatological thresholds, and moisture fields. The values of precipitation rates shown are the original values plus one and transformed with base-2 logarithm to accommodate the wide range.

All indices for Midwest ARs in Figure 8 were prone to associate with more event-average precipitation than those for the West Coast ARs. As the climatological thresholds on moisture fields became increasingly more restrictive, the indices pointed to heavier event-average precipitation rates. One conspicuous feature in Figure 8 is that $IVT+$ $IWV$-based indices are the strongest performer in both regions. As already shown in section 3.2, the combined moisture field posed the most restrictive criterion, detecting the fewest events with the shortest lifespan per event. The analysis further shows its propensity to crop out AR features with the highest precipitation rates. This is consistent with previous studies (Neiman et al., 2008; Nayak & Villarini, 2018).

Another distinct feature in Figure 8 is the disparate performance of $IVT$-based indices between the West Coast and the Midwest. $IVT$-based AR indices were associated with higher event-average precipitation in the West Coast than $IWV$-based ones. How-
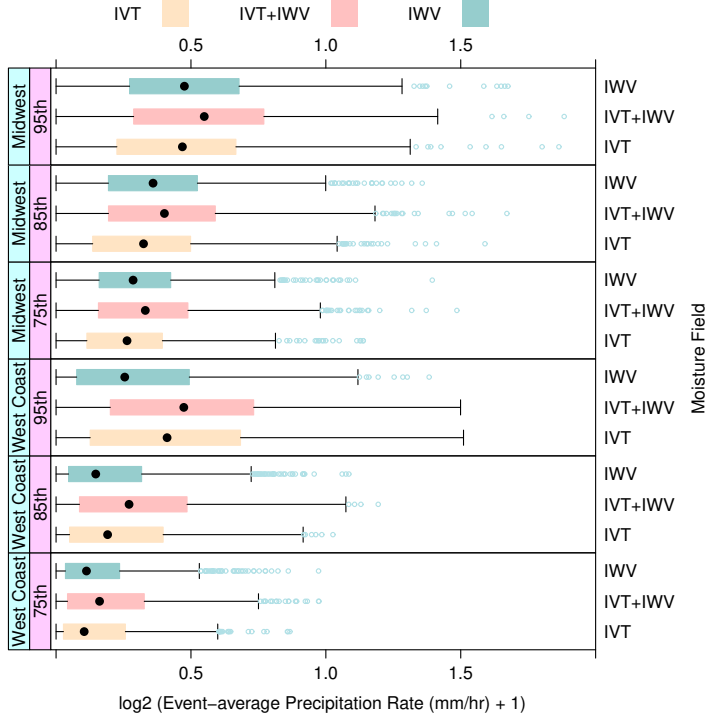
**Figure 8.** Boxplots of base-2 logarithmic transformation of event-average precipitation rate plus 1 (in mm hr$^{-1}$) over unit area according to $IVT$, $IVT + IWV$, and $IWV$-based AR indices with the same 1500-km length and 18-hr persistent duration criteria, conditional on locations and climatological thresholds labeled as percentile in 75th, 85th, and 95th.

ever, this was not the case in the Midwest. This difference is likely due to the orographic origin of precipitation on the West Coast. Compared with $IWV$, the horizontal transport of moisture expressed by the $IVT$ better indicated the vertical lifting and condensation processes upon convergence at the coastal mountains' windward side. Notably, the 95th percentile $IVT$-based West Coast AR index captured the intense orographic precipitation that $IWV$ missed.

The effects of shape and temporal criteria on the detected ARs' relations to event-average surface precipitation rate were inconclusive across different climatological thresholds and moisture fields (Figures S3 and S4). Overall, longer persistent duration criteria appeared to be associated with more average precipitation. Still, the climatological thresholds and moisture fields had the first-order influences on the event-average surface precipitation rate.
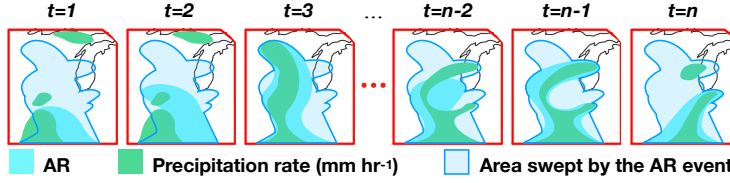
**Figure 9.** Schematic interpretation of spatial-averaged granule-level AR event-accumulated precipitation.

### 3.3.2 *Deep Analysis of Accumulated Precipitation at Fine Granularity*

Although the event-average surface precipitation is a useful metric for an AR index's overall precipitation intensity, it is even more indicative of an AR's hydrometeorological impact when combined with total event duration. Therefore, we further quantified such hydrometeorological impact using event-accumulated precipitation averaged inside a surface area swept by a detected AR. We defined, for each AR index, this area with all grid points visited at least once by the detected AR throughout its lifetime within the West Coast or Midwest region (shown in Figure 9). Given this area, we calculated the areal average of precipitation at each time step, then summed through all time steps to obtain event-accumulated precipitation for the AR event.

Figures S5 and S6, respectively, show the swept-area distributions resulted from West Coast and Midwest AR indices. The area of the West Coast region is about 1.38 times that of the Midwest region, as shown by the data upper bounds in these figures. As expected, these areas decreased with increasing climatological thresholds; the areas increased with more restrictive persistent duration thresholds; $IVT + IWV$-based indices restricted the areas to the smallest among all moisture fields, other factors being equal. Using the 75th percentile climatological thresholds, $IWV$-based indices tended to sweep a slightly broader area than $IVT$-based ones. In the Midwest region, the median areas of the 75th-percentile $IWV$-based AR indices were identical to the area upper bound; at least 50%—but fewer than 75%—of the AR events covered the entire Midwest region. The 75th-percentile $IVT$-based AR indices had median areas smaller than but very close to this upper bound. However, the areal differences between $IWV$- and $IVT$-based indices diminished at 95th percentile thresholds.

425     Figure 10a compares the event-accumulated precipitation per unit area, plus one

426     and transformed with base-2 logarithm, across the 81 West Coast AR indices using box-

427     plots. The IQRs straddle one order of magnitude, with medians at ∼3–10 mm and Q3s

428     reaching as high as ∼16 mm. The climatological and persistent duration thresholds af-

429     fected the resultant accumulated precipitation the most. We see that the more restric-

430     tive duration thresholds retained higher accumulated precipitation events when other

431     factors were fixed. The effects of changing the climatological thresholds, however, are

432     not as simple.

433     The AR indices based on the 75th percentile $IWV$ performed as well as, if not bet-

434     ter than, any other 75th percentile indices in the West Coast region. Increasing the cli-

435     matological threshold of $IWV$ beyond this point did not necessarily increase accumu-

436     lated precipitation (Figure 10a). Since the area swept by the ARs decreased (Figure S5)

437     and the event-average precipitation likely increased (e.g., Figure 8), the shorter event du-

438     ration (Figure 5) was responsible for this decline in accumulated precipitation. However,

439     among the $IVT$- and $IVT + IWV$-based indices, increased climatological thresholds

440     resulted in increased event-accumulated precipitation (Figure 10a). Even so, the event

441     duration decreased (Figure 5). Again, this could be attributed to the orographic effect

442     on intense precipitation, a prominent influencer of accumulated precipitation retained

443     by $IVT$ and $IVT + IWV$ but missed by $IWV$ with restrictive climatological thresh-

444     olds. $IVT$'s prowess in capturing the accumulated precipitation stands out with the 95th-

445     percentile threshold, considering that 95th-percentile $IVT$- and $IWV$-based indices swept

446     over similar sizes of areas (Figure S5), and $IVT$ indices tended to have shorter event du-

447     ration than $IWV$ ones (Figure 5).

448     Figure 10b compares the accumulated precipitation across the 81 Midwest AR in-

449     dices using boxplots. In general, detected Midwest ARs tended to bring twice the amount

450     of event accumulated precipitation than the West Coast ARs. The Q2s, or median val-

451     ues, are at ∼8–16 mm and Q3s extending to ∼30 mm. Similar to the West Coast AR

452     indices, more restrictive persistent duration thresholds led to higher accumulated pre-

453     cipitation. Different from the West Coast, indices based on $IWV$ outperformed those

454     based on $IVT$ or $IVT + IWV$ and resulted in the most accumulated precipitation in

455     the Midwest across all climatological thresholds.

Moreover, increasing the climatological thresholds decreased accumulated precipitation regardless of choices of moisture field. Comparison between Figures 10a and 10b shows that the choice of moisture field affected the detected AR's accumulated precipitation differently by region. AR indices with longer event duration (Figure 5) tend to be associated with more event-accumulated precipitation in the Midwest, whereas indices with larger event-average precipitation rate (Figure 8) are related to more precipitation accumulation in the West Coast. This strongly suggests that the choice of moisture field for AR indices that best expresses surface precipitation impacts on a geographical region ultimately depends on the physical understanding of the region's precipitation processes.

### 3.3.3 Seasonal Effects on Event-Accumulated Precipitation

Previous studies have demonstrated the seasonality of AR occurrence (Neiman et al., 2008; Lavers & Villarini, 2015; Nayak & Villarini, 2017). With seasonality as a point of departure, we further examined the event-accumulated precipitation. In particular, section 3.3.2 showed that the climatological threshold and moisture field choices for an AR index significantly affected its resultant accumulated precipitation. Figure 11, therefore, compares the accumulated precipitation across a group of AR indices using boxplots conditional on locations, climatological thresholds, seasons, and moisture fields. For simplicity, only indices with 1500-km length and 18-hr persistent duration thresholds are shown.

Among landfalling West Coast ARs, there was a clear seasonal cycle in the accumulated precipitation that maximized in the winter and minimized in the summer. The phase of this seasonal cycle remained unchanged across all climatological thresholds. This is consistent with the rainy and dry seasons in the West Coast, as well as the previous conclusion that warm seasons had less AR-related precipitation in the West Coast (Neiman et al., 2008). Moreover, the combined effects of climatological threshold and moisture field on the event-accumulated precipitation also had seasonality. In the warm spring and summer, $IWV$-based indices with the 75th climatological threshold led to the most accumulated precipitation. While in the fall and winter, $IVT$-based indices with the 95th threshold corresponded with the most precipitation accumulation. This was likely due to the significant orographic enhancement during the landfall of winter ARs but not summer ARs that Neiman et al. (2008) found.
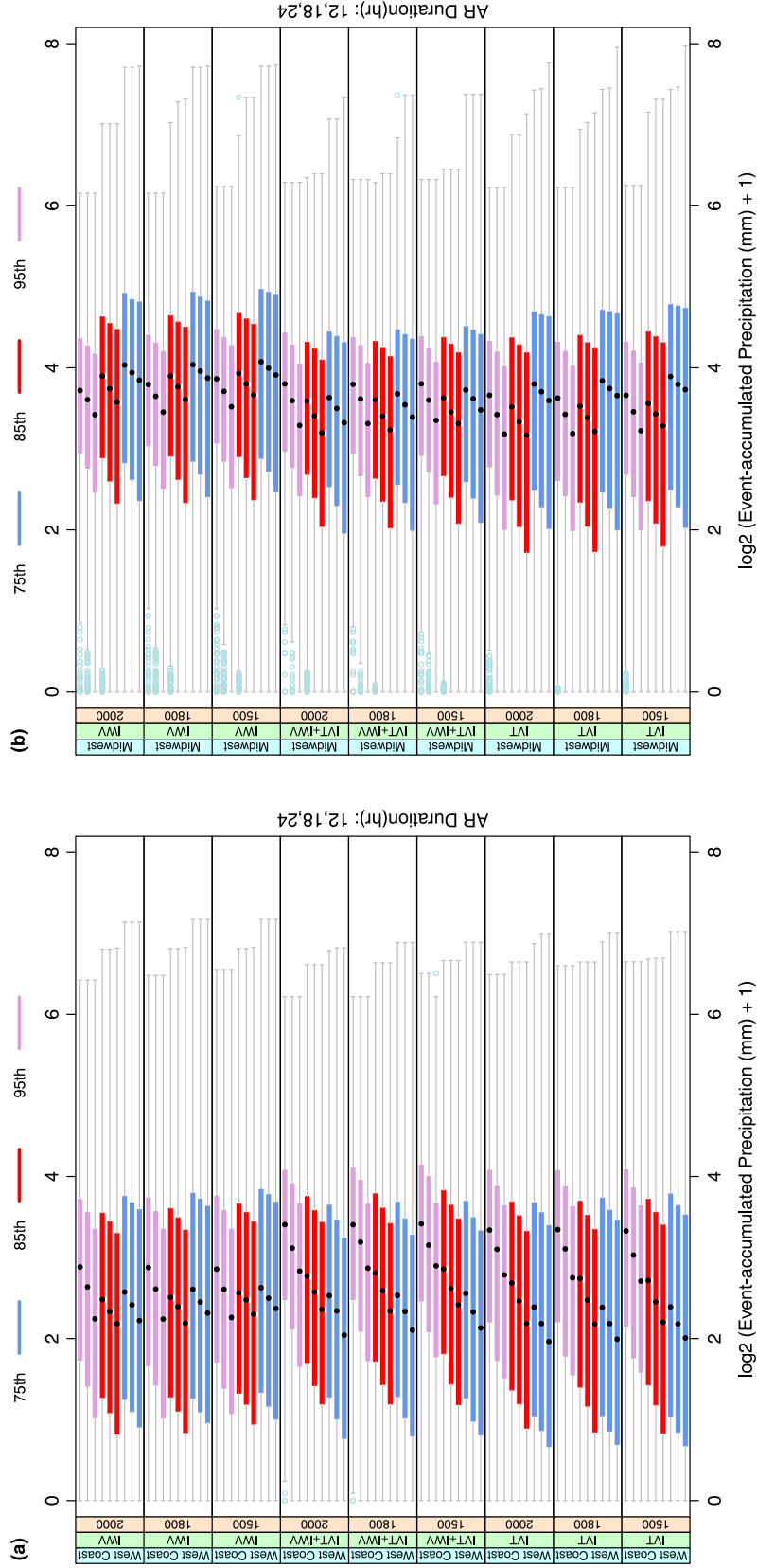
**Figure 10.** Boxplots of event-accumulated precipitation (mm) over unit area swept by ARs in the (a) West Coast and (b) Midwest. The results are base-2 log-arithmic transformation of the original values plus 1, and are conditional on nine combinations of moisture fields ($IVT$, $IWV$, or $IVT$ + $IWV$) and AR length criteria (1500, 1800, or 2000 km). Each resultant packet has nine boxplots grouped by color into three levels of climatological thresholds (75th, 85th, or 95th per-centile). Within each triplet, from bottom to top, the persistent duration thresholds increase from 12, 18, to 24 hours.
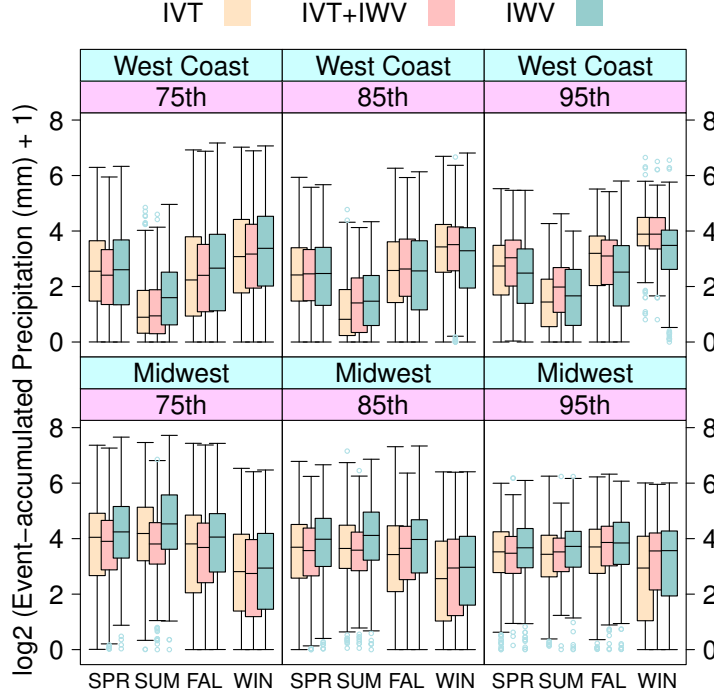
**Figure 11.** Boxplots of base-2 logarithmic transformation of event-accumulated precipitation (mm), plus 1, over unit area swept by AR in West Coast and Midwest during different seasons— spring (SPR: March–May), summer (SUM: June–August), fall (FAL: September–November), and winter (WIN: December–February)—according to $IVT$, $IVT+IWV$, and $IWV$-based AR indices with the 1500-km length and 18-hr persistent duration criteria, labeled as climate threshold in percentile 75th, 85th, or 95th in the purple box.

In contrast, among the Midwest ARs, as the climatological threshold increased, the accumulated precipitation maxima shifted from the spring-summer to the fall, and the amount in the winter increased. These suggest a dichotomy of synoptic systems associated with Midwest ARs: In addition to extratropical cyclones, the warm-month ARs received a significant amount of precipitation from maritime tropical air masses. Unlike in the West Coast, $IWV$-based Midwest AR indices were associated with the most median precipitation across all climatological thresholds and seasons.

## 4  Discussions

A single optimal AR detection algorithm expressing the surface precipitation impacts does not exist. A hint of bifurcation in our analysis started in Figure 2, in which

498    the Midwest climate thresholds underwent a greater seasonal change than that of the

499    West Coast. In section 3.3, we further found that, with meandering south-north moun-

500    tain ranges in the West Coast, $IVT$-based detection algorithms captured the intense oro-

501    graphic precipitation better than the $IWV$-based ones. This is consistent with the trend

502    to use $IVT$-based detection algorithms (Guan & Waliser, 2015). However, in the Mid-

503    west, in the absence of prominent orographic lifting, $IWV$-based AR indices were as-

504    sociated with most event-average precipitation and event-accumulated precipitation.

505    Midwest ARs recruit moisture from tropical sources such as the Gulf of Mexico,

506    Caribbean Sea, subtropical eastern North Pacific, and the Atlantic coast of Central Amer-

507    ica (Dirmeyer & Kinter, 2009, 2010). The diverse sources complicate the ARs' charac-

508    teristics (Dirmeyer & Kinter, 2010). In section 3.3.3, the seasonality of event-accumulated

509    precipitation in the Midwest shifted its peak phase from warm to cold seasons along with

510    rising climate thresholds (Figure 11), suggesting a rolling change of moisture sources and

511    baroclinicity as the seasons progressed. On the other hand, West Coast AR's peak phase

512    remained the same regardless of the changing climate threshold. There is a caveat, how-

513    ever. The West Coast's south-north geographic features are inhomogeneous. The land-

514    falling AR characteristics between the Pacific Northwest and California coast are differ-

515    ent in terms of occurrence frequency, occurrence time, and distribution and intensity of

516    related precipitation (Neiman et al., 2008). Therefore, to further refine the AR detec-

517    tion algorithms, the entire North American West Coast ARs could be divided into north-

518    west and southwest ARs. Such spatial division could better quantify ARs' contribution

519    to precipitation in each region. To illustrate this, we divided the West-Coast region at

520    California's north most boundary of 42°. Figure S7 shows that the the Northwest ARs

521    (Figure S7a) tended to yield much more event-accumulated precipitation than the South-

522    west ARs at the 75th and 85th climate thresholds, while the difference appeared to be

523    less at the 95th threshold (Figure S7b). Nevertheless, in either region, the effects of the

524    climate thresholds, persistent AR durations, and moisture fields on the resultant event-

525    accumulated precipitation are qualitatively consistent with those in the entire West-Coast

526    region (Figure 10) in section 3.3.2.

527    The combined $IVT+IWV$-based indices should be used cautiously. It is only the

528    best of both worlds when the goal is to extract snapshots of extreme precipitating events.

529    As seen in Figure 8, it led to the highest event-average precipitation rate in both West

530    Coast and Midwest. This was, however, achieved through few and short events (Figures 4a,

531 5). In fact, they performed the worst in AR–precipitation relation metrics such as *Accuracy*
532 and *F*1 *score*s (Figures 6, 7).

533 Moreover, climate thresholds and moisture fields had first-order influences on the
534 associated surface hydrometeorological impacts. However, more restrictive persistent du-
535 ration thresholds can help obtain higher event-accumulated precipitation if that is the
536 goal of detection (Figure 10).

537 The above findings appear to be robust against the inherently nonstationary time
538 series. To demonstrate this, we divided the data into two time periods: (1) January 1981–
539 December 1998 and (2) January 1999–December 2016. Similar to Figure 10, Figures S8
540 and S9 show the boxplots of event-accumulated precipitation per unit area but for the
541 81 West Coast and 81 Midwest AR indices during the first and the second periods, re-
542 spectively. The resultant distributions across all AR indices in these two separate pe-
543 riods are qualitatively similar to those in the entire study period (Figure 10). However,
544 West Coast ARs yielded more event-accumulated precipitation in the first period (Fig-
545 ure S8a) than during the second period (Figure S9a), as suggested by the median and
546 maximum values. The disparity suggests a wetter AR-related climate condition in the
547 West Coast in the first period than the second. While in the Midwest, AR-related event-
548 accumulated precipitation does not show a pronounced difference between the two pe-
549 riods (Figure S8b and S9b). Still, the maximum values might have increased in the sec-
550 ond period. The Midwest extreme AR-related event-accumulated precipitation warrants
551 detailed study in the future. Moreover, Figure S10 shows the seasonality of event-accumulated
552 precipitation conditional on climate thresholds during the two separate periods. Still,
553 the results are comparable to those in Figure 11.

554 Calculation of $IVT$-based indices requires height-dependent horizontal winds, so
555 reanalysis data are indispensable. Previous studies have suggested that AR character-
556 istics were robust across different reanalysis data (Nayak & Villarini, 2017; Ralph et al.,
557 2019). We used MERRA-2 here since Nayak and Villarini (2017) recommended high-resolution
558 products for AR impact assessments. Nevertheless, we showed that depending on the
559 goal, $IWV$ could provide optimal AR indices. When $IWV$ is useful, researchers can use
560 satellite or radiosonde water vapor measurements in lieu of reanalysis.

## 5 Conclusions

This paper investigated the optimal AR detection algorithm for expressing AR's surface precipitation effects using the MERRA-2 data for ARTMIP. We applied a data-driven approach by first asking which impacts, in which region, and in what time scale and period were of concern. We then used an algorithm combining climatological thresholds, image processing, and statistical methods to create large ensembles of AR indices for answering the questions with uncertainty quantification aided by detailed data visualization. Specifically, we varied the values of four factors—moisture fields, climatological thresholds, shape criteria, and duration thresholds—to generate an ensemble of 81 AR indices for the US West Coast and 81 indices for the Midwest regions from 1980 to 2017 (Figure 1). With CPC US Unified data, we examined the AR indices' association with the surface precipitation impacts, including the daily co-occurrence (section 3.2), event-average precipitation rate (section 3.3.1), and per-event accumulation (sections 3.3.2 and 3.3.3).

The identified Midwest ARs had more accumulated time steps (Figure 4b), longer average per-event durations (Figure 5), more event-average precipitation (Figures 8, S3, and S4), and more event-accumulated precipitation (Figures 10, S8, and S9) than the West Coast ARs. The results were sensitive to the selection of moisture field and climatological threshold in index generation. In West Coast and Midwest, $IWV$-based AR indices identified the most abundant AR event time steps and most accurately associated AR to days with precipitation. These were observed at the coarse-grain regional (Figure 6) and fine-grain grid-point scales (Figure 7). A restrictive climate threshold, such as the 95th percentile, emphasized extreme instances but limited event duration; therefore, it led to higher event-average precipitation rates. The most restrictive combination of 95th percentile $IVT+IWV$-based indices yielded the highest average precipitation (Figures 8, S5, and S6).

However, it is important to use both event-average and event-accumulated precipitation as metrics for surface hydrometeorological impacts when scrutinizing the AR indices. Therefore, we defined an area swept by each AR event (Figures 9, S5, and S6) and calculated the event-accumulated precipitation per unit area for each AR index (Figures 10, S8, and S9). On the West Coast, the 75th percentile $IWV$-based indices were associated with the most accumulated precipitation, while the 95th percentile $IVT$ captured the

accumulated precipitation the best (Figures 10a, S8a, and S9a). This could be explained by the $IVT$'s better representation of intense coastal orographic precipitation. $IWV$-based AR indices with the longest persistent duration thresholds were associated with the most accumulated precipitation in the Midwest across a range of climate thresholds (Figures 10b, S8b, and S9b). Therefore, we recommend to use $IWV$-based algorithm to identify AR-related surface precipitation in the Midwest but $IVT$-based algorithm to capture the orographically-induced precipitation in the West Coast.

Even more, the AR event-accumulated precipitation showed seasonality (Figures 11 and S10). The accumulated precipitation of all West Coast landfalling ARs had a clear seasonal cycle with the maximum in the winter and the minimum in the summer. However, for the Midwest ARs, the phase of the seasonal cycle depended on the climatological threshold. Increasing the climatological threshold from the 75th to the 95th percentile shifted the maxima from the spring–summer to fall and accentuated winter precipitation; this reflects the effects of seasonal change of moisture sources, convective instability, and atmospheric baroclincity.

In conclusion, an optimal AR detection algorithm should be adaptive to the types of impact to be addressed, the associated physical mechanisms in the affected regions, timing such as the phase in the seasonal cycle, and event durations. The systematic ensemble approach we used was made possible by distributed parallel computing with data and, specifically, the divide-and-recombine approach using the R-based DeltaRho back-ended by a Hadoop system. This study's findings provide useful information for future creators and users of AR indices who consider surface precipitation in their decision processes. Our detection algorithms and computational approach can be applied to climate model output, such as CMIP6, to explore the changes of ARs and AR-related surface precipitation impacts in climate change scenarios.

# References

Becker, R. A., Cleveland, W. S., & Shyu, M. J. (1996). The visual design and control of trellis display. *Journal of Computational and Graphical Statistics*, *5*(2), 123–155. doi: 10.1080/10618600.1996.10474701

Blamey, R. C., Ramos, A. M., Trigo, R. M., Tomé, R., & Reason, C. J. (2018). The influence of atmospheric rivers over the South Atlantic on winter rainfall in South Africa. *Journal of Hydrometeorology*, *19*(1), 127–142. doi: 10.1175/JHM-D-17-0111.1

Chen, M., Shi, W., Xie, P., Silva, V. B., Kousky, V. E., Higgins, R. W., & Janowiak, J. E. (2008). Assessing objective techniques for gauge-based analyses of global daily precipitation. *J. Geophys. Res. Atmos.*, *113*(4), 1–13. doi: 10.1029/2007JD009132

Chen, X., Leung, L. R., Gao, Y., Liu, Y., Wigmosta, M., & Richmond, M. (2018). Predictability of Extreme Precipitation in Western U.S. Watersheds Based on Atmospheric River Occurrence, Intensity, and Duration. *Geophys. Res. Lett.*, *45*(21), 11,693–11,701. doi: 10.1029/2018GL079831

Cleveland, W. S., & Hafen, R. (2014). Divide and recombine (D&R): Data science for large complex data. *Statistical Analysis Data Mining*, *7*(6), 425–433. doi: 10.1002/sam.11242

Cleveland, W. S., & McGill, R. (1984). Graphical perception: Theory, experimentation, and application to the development of graphical methods. *Journal of the American Statistical Association*, *79*(387), 531–554. doi: 10.1080/01621459.1984.10478080

Daly, C., Halbleib, M., Smith, J. I., Gibson, W. P., Doggett, M. K., Taylor, G. H., . . . Pasteris, P. P. (2008). Physiographically sensitive mapping of climatological temperature and precipitation across the conterminous United States. *Int. J. Climatol.*, *28*(15), 2031–2064. doi: https://doi.org/10.1002/joc.1688

Dettinger, M. D. (2011). Climate change, atmospheric rivers, and floods in California - a multimodel analysis of storm frequency and magnitude changes. *Journal of the American Water Resources Association*, *47*(3), 514–523. doi:

657    10.1111/j.1752-1688.2011.00546.x

658  Dettinger, M. D.    (2013).    Atmospheric rivers as drought busters on the U.S. West
659         Coast.    *Journal of Hydrometeorology*, *14*(6), 1721–1732.    doi: 10.1175/JHM-D
660         -13-02.1

661  Dettinger, M. D., Ralph, F. M., Das, T., Neiman, P. J., & Cayan, D. R.    (2011).    At-
662         mospheric Rivers, Floods and the Water Resources of California.    *Water*, *3*(2),
663         445–478. doi: 10.3390/w3020445

664  Dirmeyer, P. A., & Kinter, J. L.    (2009).    The "Maya Express": Floods in the U.S.
665         Midwest. *EOS Transactions*, *90*(12), 101–102. doi: 10.1029/2009EO120001

666  Dirmeyer, P. A., & Kinter, J. L.    (2010).    Floods over the U.S. midwest: A regional
667         water cycle perspective.    *Journal of Hydrometeorology*, *11*(5), 1172–1181.    doi:
668         10.1175/2010JHM1196.1

669  Eiras-Barca, J., Brands, S., & Miguez-Macho, G.    (2016).    Seasonal variations in
670         North Atlantic atmospheric river activity and associations with anomalous pre-
671         cipitation over the Iberian Atlantic margin.    *Journal of Geophysical Research
672         Atmosphere*, *121*(2), 931–948. doi: 10.1002/2015JD023379

673  Gelaro, R., McCarty, W., Suárez, M. J., Todling, R., Molod, A., Takacs, L., . . .
674         Zhao, B.    (2017).    The modern-era retrospective analysis for research and ap-
675         plications, version 2 (MERRA-2). *Journal of Climate*, *30*(14), 5419–5454.  doi:
676         10.1175/JCLI-D-16-0758.1

677  Gershunov, A., Shulgina, T., Ralph, F. M., Lavers, D. A., & Rutz, J. J.    (2017).
678         Assessing the climate-scale variability of atmospheric rivers affecting west-
679         ern North America.    *Geophysical Research Letters*, *44*(15), 7900–7908.    doi:
680         10.1002/2017GL074175

681  Gibson, P. B., Waliser, D. E., Lee, H., Tian, B., & Massoud, E.    (2019).    Climate
682         model evaluation in the presence of observational uncertainty: Precipitation
683         indices over the contiguous United States. *Journal of Hydrometeorology*, *20*(7),
684         1339–1357. doi: 10.1175/JHM-D-18-0230.1

685  Guan, B., Molotch, N. P., Waliser, D. E., Fetzer, E. J., & Neiman, P. J.    (2010).
686         Extreme snowfall events linked to atmospheric rivers and surface air temper-
687         ature via satellite measurements.    *Geophysical Research Letters*, *37*(20).    doi:
688         10.1029/2010GL044696

689  Guan, B., Molotch, N. P., Waliser, D. E., Fetzer, E. J., & Neiman, P. J.    (2013).

The 2010/2011 snow season in California's Sierra Nevada: Role of atmospheric rivers and modes of large-scale variability. *Water Resources Research*, *49*(10), 6731–6743. doi: 10.1002/wrcr.20537

Guan, B., & Waliser, D. E. (2015). Detection of atmospheric rivers: Evaluation and application of an algorithm for global studies. *Journal of Geophysical Research Atmosphere*, *120*(24), 12,514–12,535. doi: 10.1002/2015JD024257

Hastie, T., & Stuetzle, W. (1989). Principal Curves. *Journal of the American Statistical Association*, *84*(406), 502–516. doi: 10.1080/01621459.1989.10478797

Hastie, T., Tibshirani, R., & Friedman, J. (2001). *The elements of statistical Learning: Data mning, inference, and prediction.* Springer, New York, NY. doi: 10 .1007/978-0-387-84858-7

Higgins, R., Shi, W., Yarosh, E., & Joyce, R. (2000). *Improved United States precipitation quality control system and analysis. NCEP/Climate Prediction Center ATLAS 7.*

Lavers, D. A., & Villarini, G. (2013). Atmospheric rivers and flooding over the central United States. *Journal of Climate*, *26*(20), 7829–7836. doi: 10.1175/JCLI -D-13-00212.1

Lavers, D. A., & Villarini, G. (2015). The contribution of atmospheric rivers to precipitation in Europe and the United States. *Journal of Hydrology*, *522*, 382– 390. doi: 10.1016/j.jhydrol.2014.12.010

Lavers, D. A., Villarini, G., Allan, R. P., Wood, E. F., & Wade, A. J. (2012). The detection of atmospheric rivers in atmospheric reanalyses and their links to British winter floods and the large-scale climatic circulation. *Journal of Geophysical Research Atmospheres*, *117*(20). doi: 10.1029/2012JD018027

Leung, L. R., & Qian, Y. (2009). Atmospheric rivers induced heavy precipitation and flooding in the western U.S. simulated by the WRF regional climate model. *Geophysical Research Letters*, *36*(3), L03820. doi: 10.1029/2008GL036445

Little, K., Kingston, D. G., Cullen, N. J., & Gibson, P. B. (2019). The Role of Atmospheric Rivers for Extreme Ablation and Snowfall Events in the Southern Alps of New Zealand. *Geophysical Research Letters*, *46*(5), 2761–2771. doi: 10.1029/2018GL081669

Luo, Q., & Tung, W.-w. (2015). Case study of moisture and heat budgets within at-

mospheric rivers. *Monthly Weather Review*, *143*(10), 4145–4162. doi: 10.1175/ MWR-D-15-0006.1

Nayak, M. A., & Villarini, G. (2017). A long-term perspective of the hydroclimato-logical impacts of atmospheric rivers over the central United States. *Water Resources Research*, *53*(2), 1144–1166. doi: 10.1002/2016WR019033

Nayak, M. A., & Villarini, G. (2018). Remote sensing-based characterization of rain-fall during atmospheric rivers over the central United States. *Journal of Hydrology*, *556*, 1038–1049. doi: 10.1016/j.jhydrol.2016.09.039

NCAR CDG. (2019). *3-hourly MERRA2 IVT, uIVT, vIVT, IWV data computed for ARTMIP.* (last access: 24 January 2019) doi: 10.5065/D62R3QFS

NCAR CDG. (2021). *ARTMIP Tier 1 Catalogues.* (last access: 1 January 2021) doi: 10.5065/D6R78D1M

Neiman, P. J., Ralph, F. M., Wick, G. A., Lundquist, J. D., & Dettinger, M. D. (2008). Meteorological characteristics and overland precipitation impacts of atmospheric rivers affecting the West coast of North America based on eight years of SSM/I satellite observations. *Journal of Hydrometeorology*, *9*(1), 22–47. doi: 10.1175/2007JHM855.1

Neiman, P. J., White, A. B., Ralph, F. M., Gottas, D. J., & Gutman, S. I. (2009). A water vapour flux tool for precipitation forecasting. *Proceedings of the Institution of Civil Engineers: Water Management*, *162*(2), 83–94. doi: 10.1680/ wama.2009.162.2.83

NOAA/OAR/ESRL PSL. (2021). *CPC US Unified Precipitation https://psl.noaa.gov/data/gridded/data.unified.daily.conus.html.* (last access: 1 January 2021)

O'Brien, T. A., Payne, A. E., Shields, C. A., Rutz, J., Brands, S., Castellano, C., . . . Zhou, Y. (2020). Detection uncertainty matters for understanding atmospheric rivers. *Bulletin of the American Meteorological Society*, *101*(6), E790-E796. doi: 10.1175/bams-d-19-0348.1

Payne, A. E., & Magnusdottir, G. (2016). Persistent landfalling atmospheric rivers over the west coast of North America. *Journal of Geophysical Research Atmosphere*, *121*(22), 13,287–13,300. doi: 10.1002/2016JD025549

Ralph, F. M., Coleman, T., Neiman, P. J., Zamora, R. J., & Dettinger, M. D. (2013). Observed impacts of duration and seasonality of atmospheric-river

landfalls on soil moisture and runoff in coastal Northern California. *Journal of Hydrometeorology*, *14*(2), 443–459. doi: 10.1175/JHM-D-12-076.1

Ralph, F. M., Dettinger, M. D., Cairns, M. M., Galarneau, T. J., & Eylander, J. (2018). Defining "Atmospheric River": how the glossary of meteorology helped resolve a debate. *Bulletin of the American Meteorological Society*, *99*(4), 837–839. doi: 10.1175/BMAS-D-17-0157.1

Ralph, F. M., Neiman, P. J., Kiladis, G. N., Weickmann, K., & Reynolds, D. W. (2011). A multiscale observational case study of a Pacific atmospheric river exhibiting tropical-extratropical connections and a mesoscale frontal wave. *Monthly Weather Review*, *139*(4), 1169–1189. doi: 10.1175/2010MWR3596.1

Ralph, F. M., Neiman, P. J., & Rotunno, R. (2005). Dropsonde observations in low-level jets over the Northeastern Pacific Ocean from CALJET-1998 and PACJET-2001: Mean vertical-profile and atmospheric-river characteristics. *Monthly Weather Review*, *133*(4), 889–910. doi: 10.1175/MWR2896.1

Ralph, F. M., Neiman, P. J., & Wick, G. A. (2004). Satellite and CALJET aircraft observations of atmospheric rivers over the Eastern North Pacific ocean during the winter of 1997/98. *Monthly Weather Review*, *132*(7), 1721–1745. doi: 10.1175/1520-0493(2004)132⟨1721:SACAOO⟩2.0.CO;2

Ralph, F. M., Neiman, P. J., Wick, G. A., Gutman, S. I., Dettinger, M. D., Cayan, D. R., & White, A. B. (2006). Flooding on California's Russian River: Role of atmospheric rivers. *Geophysical Research Letters*, *33*(5), L13801. doi: 10.1029/2006GL026689

Ralph, F. M., Wilson, A. M., Shulgina, T., Kawzenuk, B., Sellars, S., Rutz, J. J., . . . Wick, G. A. (2019). ARTMIP-early start comparison of atmospheric river detection tools: how many atmospheric rivers hit northern California's Russian River watershed? *Climate Dynamics*, *52*(7-8), 4973–4994. doi: 10.1007/s00382-018-4427-5

Rutz, J. J., Shields, C. A., Lora, J. M., Payne, A. E., Guan, B., Ullrich, P., . . . Viale, M. (2019). The Atmospheric River Tracking Method Intercomparison Project (ARTMIP): Quantifying uncertainties in atmospheric river climatology. *Journal of Geophysical Research: Atmospheres*, *124*, 13,777–13,802. doi: 10.1029/2019JD030936

Rutz, J. J., & Steenburgh, W. J. (2012). Quantifying the role of atmospheric rivers

in the interior western United States. *Atmospheric Science Letters*, *13*(4), 257–261. doi: 10.1002/asl.392

Rutz, J. J., Steenburgh, W. J., & Ralph, F. M.   (2014).   Climatological characteristics of atmospheric rivers and their inland penetration over the western United States.   *Monthly Weather Review*, *142*(2), 905–921.   doi: 10.1175/MWR-D-13-00168.1

Sellars, S. L., Gao, X., & Sorooshian, S.   (2015).   An object-oriented approach to investigate impacts of climate oscillations on precipitation: A western United States case study.   *Journal of Hydrometeorology*, *16*(2), 830–842. doi: 10.1175/JHM-D-14-0101.1

Shields, C. A., Rutz, J. J., Leung, L.-Y., Ralph, F. M., Wehner, M., Kawzenuk, B., . . . Nguyen, P.   (2018).   Atmospheric River Tracking Method Intercomparison Project (ARTMIP): project goals and experimental design. *Geoscientific Model Development*, *11*, 2455–2474. doi: 10.5194/gmd-11-2455-2018

Tung, W.-w., Barthur, A., Bowers, M. C., Song, Y., Gerth, J., & Cleveland, W. S.   (2018).   Divide and recombine (D&R) data science projects for deep analysis of big data and high computational complexity.   *Japanese Journal of Statistics and Data Science*, *1*(1), 139–156. doi: 10.1007/s42081-018-0008-4

Wick, G. A., Neiman, P. J., & Ralph, F. M.   (2013).   Description and validation of an automated objective technique for identification and characterization of the integrated water vapor signature of atmospheric rivers.   *IEEE Transactions on Geoscience and Remote Sensing*, *51*(4), 2166–2176.   doi: 10.1109/TGRS.2012.2211024

Wolter, K., & Timlin, M. S.   (1993).   *Monitoring enso in coads with a seasonally adjusted principal component index.*   Paper presented at the 17th Climate Diagnostics Workshop, NOAA/NMC/CAC, NSSL, Oklahoma Clim. Survey, CIMMS and the School of Meteor., Univ. of Oklahoma, Norman, OK.

Xie, P., Yatagai, A., Chen, M., Hayasaka, T., Fukushima, Y., Liu, C., & Yang, S. (2007).   A gauge-based analysis of daily precipitation over East Asia.   *J. Hydrometeorol.*, *8*(3), 607–626. doi: 10.1175/JHM583.1

Zhu, Y., & Newell, R. E.   (1998).   A proposed algorithm for moisture fluxes from atmospheric rivers.   *Monthly Weather Review*, *126*(3), 725–735.   doi: 10.1175/1520-0493(1998)126⟨0725:APAFMF⟩2.0.CO;2